Applied Surface Science 720 (2026) 165300

Contents lists available at ScienceDirect

Applied Surface Science

journal homepage: www.elsevier.com/locate/apsusc

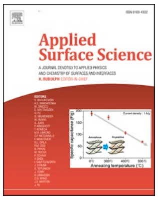

Full Length Article

Revealing the dual role of nanoparticle size and surface ligands in plasmon-enhanced photocatalysis of Au/TiO_2 nanorods

Špela Slapničar [a], Maja Caf [b,c], Slavko Kralj [b,c], Gregor Žerjav [a], Albin Pintar [a,*]

[a] Department of Inorganic Chemistry and Technology, National Institute of Chemistry, Hajdrihova ulica 19, SI-1001 Ljubljana, Slovenia
[b] Department of Materials Synthesis, Jožef Stefan Institute, Jamova cesta 39, SI-1000 Ljubljana, Slovenia
[c] Faculty of Pharmacy, University of Ljubljana, Aškerčeva cesta 7, SI-1000 Ljubljana, Slovenia

ARTICLE INFO

Keywords:
Heterogeneous photocatalysis
Titanate nanorods
gold NPs
Wet impregnation
Localized surface plasmon resonance effect

ABSTRACT

The development of plasmon-enhanced TiO_2 photocatalysts offers exciting opportunities for the use of visible light in environmental and energy-related applications. A key parameter that determines their performance is the size and distribution of the plasmonic metal nanoparticles (NPs), which strongly influence charge separation, light absorption and interfacial chemistry. In this work, we have systematically investigated the role of Au NPs size on the structural, electronic and photocatalytic properties of hydrothermally synthesized TiO_2 nanorods (TNR). Au NPs with well-controlled diameters in the range of 10–50 nm were uniformly deposited on the TNR surfaces, which was confirmed by electron microscopy and elemental mapping. UV–Vis diffuse reflectance spectra confirmed the absorption of localized surface plasmon resonance (LSPR) in the visible region, with peak positions depending on both the size of the NPs and the presence of Na-citrate residues from the synthesis. Supplementary spectroscopic analyses showed that citrate residues altered the surface chemistry, impaired charge transfer and partially blocked active sites. Photoluminescence and time-correlated single photon counting measurements revealed that Au decoration effectively suppressed the recombination of electrons and holes and prolonged the lifetime of charge carriers, while electron paramagnetic resonance spectroscopy showed improved stabilization of Ti^{3+} centers and oxygen vacancies upon visible-light irradiation. Photocatalytic tests, evaluated by the generation of reactive oxygen species and the degradation of bisphenol A (BPA), showed that the activity increased with decreasing NPs size. The sample with the smallest Au NPs showed the highest reactivity and achieved a BPA degradation of $\sim$40 within 4 h. Thus, it clearly outperformed both the larger Au-decorated TNR and the untreated TNR reference sample. Nevertheless, residual citrate limited the overall efficiency by hindering charge transport and surface reactivity. These findings provide a pathway for the rational design of more efficient plasmonic photocatalysts by controlling NP size and removing synthesis by-products.

1. Introduction

The degradation of bisphenol A (BPA) has become a pressing issue in recent years, as BPA is an antioxidant that is not biodegradable, is highly resistant to chemical degradation and poses a risk to human and animal health. One of the most important areas of research is therefore the development of effective methods for the degradation of BPA in contaminated wastewater. Around 3 million tonnes of BPA waste are produced every year, although some sources speak of up to 7 million tonnes [1]. This shows that the problem is indeed very serious, as BPA is considered an endocrine disruptor. Researchers at an institute in China conducted a study on the occurrence of BPA. They analyzed urine samples and detected BPA in almost all samples tested, which means that BPA is widespread [2,3]. High concentrations of BPA have been found in in landfill leachates, reaching up to 17.2 mg/L [4,5]. Conventional water treatment methods cannot completely remove BPA, which is why advanced oxidation processes (AOPs), such as heterogeneous photocatalysis, are used [6,7]. Photocatalysis has proven to be a promising strategy to tackle global challenges such as environmental remediation. TiO_2 has long been recognized as one of the most effective photocatalytic materials due to its high chemical stability, low cost and strong oxidizing power under UV irradiation. However, its practical use is hindered by its large band gap (3.2 eV for anatase) [8–10], which limits its absorption to only about 3–4 % of the solar spectrum [11,12],

---

* Corresponding author.
E-mail address: albin.pintar@ki.si (A. Pintar).

https://doi.org/10.1016/j.apsusc.2025.165300
Received 13 October 2025; Received in revised form 27 October 2025; Accepted 17 November 2025
Available online 21 November 2025
0169-4332/© 2025 The Author(s). Published by Elsevier B.V. This is an open access article under the CC BY license (http://creativecommons.org/licenses/by/4.0/).

and by the rapid recombination of photogenerated electron-hole pairs [13]. To extend its activity into the visible region and improve charge separation, various modification strategies have been explored, of which the incorporation of noble metal nanoparticles (NPs), particularly Au. Au NPs are stable and non-toxic, which is why they have attracted considerable interest [14,15]. The size and shape of the metal NPs have proven to be key parameters in the development of TiO_2-based catalysts. One of the most important properties affecting the photocatalytic performance of these materials is the localized surface plasmon resonance (LSPR), which results from the coherent oscillation of free electrons in plasmonic NPs and enables a more efficient interaction with the TiO_2 support.

The increase in light absorption due to LSPR can be detected by UV–Vis spectrophotometry, where an increase in absorption occurs (a peak in the UV–Vis diffuse reflectance spectrum, e.g. for Au/TiO_2). This phenomenon results from changes in the electric field at the surface of the NP and enables more efficient electron transfer between the metal and the semiconductor. In larger NPs, the LSPR shifts, which means that the light spectrum expands to higher wavelengths (red shift), which can influence the photocatalytic properties of the catalyst. In NPs smaller than 10 nm, the plasmonic resonance occurs at lower wavelengths (400–500 nm), while in larger plasmonic NPs (>50 nm) the resonance shifts towards 600 nm. This changes the ability of the catalyst to absorb certain parts of the solar spectrum, which affects its performance under real environmental conditions, e.g. in the degradation of the organic pollutant BPA. Smaller NPs have a larger specific surface area and provide more active sites for reactions, which increases the rate of photocatalytic processes. However, small NPs can also lead to a higher recombination rate of electrons and holes, which reduces the efficiency of the catalyst. Larger particles can separate charges more effectively as they act as electron traps, but they have fewer active sites per unit mass. In addition, larger NPs can form aggregates that restrict the access of light to the active sites, further reducing photocatalytic activity. The size of Au NPs is closely related to the contact distance to the TiO_2 support. For smaller metal NPs (2.8 nm) [16], the contact distance was larger than the NP diameter, which allowed for better electron transfer and a larger surface area for the absorption of light and pollutants. This increased surface area allows for more effective injection of photogenerated electrons into TiO_2 when irradiated with visible light, which increases photocatalytic activity. However, as the size of the NPs increases, the contact distance decreases, which can have a negative effect on the efficiency of electron transfer [16]. The deposition of smaller NPs on the catalyst support enables a more uniform dispersion on the TiO_2 surface. Some studies have shown that smaller Au particles are more active compared to larger Au NPs [17,18], but Yoo et al. [19] have shown that the LSPR effect occurs with larger Au NPs, which is crucial for extending the lifetime of charge carriers and leads to improved photocatalytic activity.

Although many studies have reported visible-light photocatalysis in Au/TiO_2 systems, particularly for the degradation of bisphenol A, several key aspects remain insufficiently understood. Most research has focused on optimising Au loading or correlating average nanoparticle size with overall activity [20,21], while the interplay between nanoparticle size, surface chemistry, and charge-transfer efficiency has received much less attention. In particular, the influence of residual surface ligands from colloidal synthesis routes on the plasmonic and photocatalytic behaviour of Au/TiO_2 catalysts has not been systematically addressed. In this work, we systematically investigate the size-dependent effects of Au nanoparticles on the photocatalytic degradation of BPA under visible-light irradiation. Au nanoparticles with controlled sizes (10–50 nm) were synthesized using Na-citrate and immobilized on TiO_2 nanorods (TNR). This study uniquely combines precise control of Au nanoparticle size with a detailed assessment of residual Na-citrate species, offering a dual mechanistic perspective rarely explored in previous Au/TiO_2 photocatalyst studies. Advanced spectroscopic analyses provide direct evidence of how surface residues influence charge separation, Ti^{3+} stabilization, and plasmon-induced electron transfer. By correlating nanoparticle size, surface chemistry, and photocatalytic activity, this work provides new insight into how Au/TiO_2 plasmonic interfaces can be rationally engineered. The findings offer practical guidance for designing efficient and stable photocatalysts capable of operating under natural sunlight and in real wastewater treatment applications.

2. Experimental

2.1. Materials

Sodium hydroxide (NaOH, ≥98 %, Merck), hydrochloric acid (HCl, fuming 37 %, ≤1 ppm free chlorine, Merck), hydrogen tetrachloroaurate trihydrate ($HAuCl_4 \cdot 3H_2O$, 99.99 %, Alfa Aesar), citric acid monohydrate, 99.5–100.5 %, Sigma Aldrich), absolute ethanol (C_2H_5OH, ≥99.5 %, Carlo Erba reagents), coumarin (COUM, ≥98 %, Thermo Fisher), 2,2′-azino-bis-(3-ethylbenzothiazoline-6-sulfonic acid) cation ($ABTS^{\bullet +}$, ≥98 %, Sigma Aldrich), potassium persulfate ($K_2S_2O_8$, ≥99 %, Sigma Aldrich) and bisphenol A (BPA, ≥99 %, Sigma Aldrich) were used as received. TiO_2 precursor DT-51 was donated from the company CristalACTiV™. All aqueous solutions used in this work were prepared with ultrapure water (18.2 MΩ cm) and kept in the dark at 4 °C.

2.2. Catalyst synthesis

TNR were prepared by hydrothermal synthesis, as described in our previous publications [22,23]. Gold NPs of different sizes were synthesized using various approaches, which are described in detail in the following paragraphs.

The synthesis of Au NPs with an average diameter of approximately 10 nm was adapted from the protocol described by Ojea-Jiménez et al. [24]. Briefly, 102 mL of 2.45 mM NaOH and 2.1 mL of 0.34 M Na-citrate were mixed and transferred into a round-bottom flask equipped with a reflux condenser. The solution was heated to boiling in an oil bath. Upon reaching the boiling point, 2 mL of 0.066 M $HAuCl_4 \cdot 3H_2O$ was rapidly injected, resulting in an immediate color change from colorless to black, followed by a gradual transition to a characteristic wine-red color, indicating the formation of gold NPs. After completion of the reaction, the colloidal suspension was cooled to room temperature in an ice bath and subsequently washed with distilled water to remove excess Na-citrate, yielding citrate-stabilized gold NPs with a mean diameter of 10 nm, hereafter referred to as Au1.

Spherical gold NPs with distinct diameters ranging from 20 to 50 nm were synthesized via a multi-step seed-mediated growth method, adapted from the procedures reported by Bastús et al. and our work [25,26]. Aqueous stock solutions of Na-citrate (2.2 mM and 60 mM) and $HAuCl_4 \cdot 3H_2O$ (25 mM) were first prepared.

Seed preparation: For the synthesis of gold seed NPs, 37.5 mL of 2.2 mM Na-citrate was heated to boiling in a 100 mL round-bottom flask equipped with a reflux condenser and immersed in an oil bath. Once boiling, 0.25 mL of the 25 mM $HAuCl_4 \cdot 3H_2O$ solution was rapidly added under vigorous stirring for 1 min, producing a light pink coloration indicative of seed formation. The reaction mixture was then allowed to cool to 90 °C at ambient conditions (room temperature).

First growth step (Au2): Once cooled, the seed solution was returned to the oil bath and maintained at 90 °C, with the stirring rate reduced to 600 rpm. To promote further NP growth, 0.25 mL of 25 mM $HAuCl_4 \cdot 3H_2O$ was added, followed by two additions of the same volume at 10-minute intervals (three additions in total). This step yielded gold NPs with an average diameter of 20 nm, hereafter referred to as Au2.

Second growth step (Au3): To further increase NP size, a fresh growth medium was prepared by heating a mixture of 13.25 mL of distilled water and 0.5 mL of 60 mM Na-citrate to 90 °C. Once at temperature, this diluted Na-citrate solution was added to the Au2 suspension, followed by three sequential 0.25 mL additions of 25 mM $HAuCl_4 \cdot 3H_2O$ at

10-minute intervals. This produced NPs with a mean diameter of 31 nm, designated as Au3.

Subsequent growth steps (Au4 and Au5): The dilution–growth cycle was repeated twice more to obtain progressively larger NPs: Au4, with an average diameter of 37 nm, and Au5, with an average diameter of 53 nm.

Purification: Following the final growth step, all NP suspensions were purified by repeated washing with distilled water to remove excess Na-citrate.

A wet impregnation technique was used to deposit Au NPs on TNR. The preparation procedure was similar to that described in our previous articles [27,28]. The TNR support was ultrasonically dispersed in 250 mL ethanol for 10 min. Then a suspension of Au NPs was added in an amount that resulted in a metal loading of 1.0 wt%. The suspension was then stirred continuously for 20 h. The solvent was then evaporated using a rotary evaporator and the resulting material was dried at 80 °C for 18 h. The sample was then calcined at 300 °C for 2 h with a heating ramp of 150 °C per hour [29]. We prepared five different Au/TiO_2 catalysts with different sizes of Au NPs: (i) TNR + Au1, (ii) TNR + Au2, (iii) TNR + Au3, (iv) TNR + Au4, and (v) TNR + Au5.

2.3. Catalyst characterization

The morphology and chemical composition of the investigated materials were analyzed using a transmission electron microscope (TEM, JEM-2100, JEOL Inc.) equipped with energy-dispersive X-ray spectroscopy (EDXS, JED-2300 EDS) and a scanning electron microscope (SEM, SUPRA 35 VP, Carl Zeiss) with energy-dispersive X-ray spectroscopy (SEM-EDXS, Inca 400, Oxford Instruments). For each NP type, TEM grids were prepared by depositing a few drops of the diluted sample onto the grid, followed by air drying. NP size distributions were determined from TEM images using ImageJ software, based on measurements of 100 individual particles (N = 100). For SEM-EDXS analysis, the powdered catalysts were attached to aluminum holder with double-sided carbon tape and gently blown out with compressed air to remove loose particles. The elemental composition of the photocatalysts was determined using a CHNS elemental analyzer (2400 Series II, Perkin Elmer, USA). The N_2-physisorption measurements were carried out with a Micromeritics TriStar II 3020 analyzer. Prior to the measurements, the catalysts were degassed under N_2 (purity 6.0) using a Micromeritics SmartPrep unit at 90 °C for 60 min and 180 °C for 240 min (calcined samples), or at 80 °C for 1260 min (non-calcined samples). The specific surface areas (S_{BET}) were calculated by the Brunauer-Emmett-Teller (BET) method, while the total pore volume (V_{pore}) and pore size (d_{pore}) distribution were determined from the desorption isotherms using the Barrett-Joyner-Halenda (BJH) method.

The crystallinity and phase composition of the synthesized catalysts were analyzed by powder X-ray diffraction (XRD) using a PANalytical X′Pert Pro diffractometer with Cu Kα1 radiation ($\lambda = 0.15406$ nm). The catalysts were scanned over a 2θ range of 5-90° with a step size of 0.033° and a counting time of 100 s per step. The diffractograms were evaluated using the HighScore Plus software (version 4.9).

UV–Vis diffuse reflectance (DR) spectroscopy was used to analyze the light absorption properties of the samples at different wavelengths. Spectra were recorded using a Perkin Elmer Lambda 650 UV–Vis spectrophotometer equipped with a Praying Mantis diffuse reflectance accessory (DRP-SAP, Harrick), to analyze powdered samples. Measurements were performed at room temperature over a wavelength range of 200–900 nm, with a scan rate of 266.75 nm/min.

Photoluminescence (PL) measurements were performed with a Perkin Elmer LS 55 fluorescence spectrometer equipped with a solid-sample holder. The excitation wavelength was set to 300 nm, with excitation and emission slit widths of 5 nm and 7.5 nm, respectively. The spectra were recorded between 300 and 600 nm at a scanning speed of 200 nm/min.

Time-correlated single photon counting (TCSPC) measurements were performed using a Horiba Fluorolog-QM spectrofluorometer equipped with a DeltaDiode$^{\mathrm{TM}}$ picosecond pulsed laser light source (nominal excitation wavelength of 495 nm) and a PPD detector (model 850). The slits in the emission monochromator were set to 8 nm, and the time window was set to 200 ns with 4096 channels. The emission response was monitored at 350, 550, and 600 nm. A Ludox SM-30 solution of colloidal silica was used as a reference to determine the instrument response function (IRF), which was used to calculate the lifetimes of the charge carriers with the FelixFL spectroscopy software.

The chemical composition of the samples was also analyzed using attenuated total reflection Fourier-transform infrared spectroscopy (ATR-FTIR) on a Perkin Elmer Frontier FTIR spectrometer. Each spectrum was recorded as an average of 32 scans with a spectral resolution of 4 cm^{-1} in the 4000–400 cm^{-1} range.

The surface properties were analyzed using a Pyris 1 TGA instrument (Perkin Elmer, USA). The samples were first stabilized in air at 40 °C for 5 min. They were then heated to 600 °C under a stream of air at a rate of 10 °C min^{-1} and held at the target temperature for 5 min.

The electron paramagnetic resonance (EPR) measurements were performed using a benchtop EPR spectrometer (Adani, model CMS 8400) operating at a microwave frequency of 9.4 GHz. The measurements were performed at a central magnetic field of 338 mT, with a sweep width of 40 or 200 mT, a modulation amplitude of 450 μT, a microwave attenuation of 15 dB, and a gain factor of 2×10^3. Each sample was measured three times consecutively to obtain averaged spectra. For visible-light illumination, we used a Schott KL 2500 LED (energy spectrum is shown in Fig. S1) light source and irradiated the samples through the side channel of the EPR spectrometer for 15 min before measuring the spectra.

2.4. Evaluation of the photocatalytic activity

The formation of various reactive oxygen species (ROS) under irradiation with visible light was investigated using specific probe molecules. A 200 mg L^{-1} aqueous solution of coumarin (COUM) was used to monitor the generation rate of hydroxyl radicals ($OH^{\bullet}$). In addition, an aqueous $ABTS^{\bullet+}$ solution was prepared by dissolving 17.2 mg of 2,2′-azino-bis(3-ethylbenzothiazoline-6-sulfonic acid) diammonium salt ($ABTS^{\bullet+}$) and 3.3 mg of $K_2S_2O_8$ in a 5 mL flask to monitor the generation of electrons (e^-) and superoxide anion radicals ($O_2^{\bullet-}$).

The reactions were carried out in a glass batch reactor containing 50 mL of the coumarin solution and 10 mg of catalyst. Prior to irradiation, the suspension was kept in the dark for 20 min to ensure adsorption–desorption equilibrium. The system was then irradiated with visible light using a Schott KL 2500 LED light source. Samples were taken at predetermined time intervals, filtered through 0.2 μm membrane filters, and stored in Eppendorf tubes for analysis. The formation of 7-hydroxycoumarin (7-OHC), a fluorescent product of the reaction between $OH^{\bullet}$ radicals and coumarin, was analyzed using a UV–Vis photoluminescence spectrometer (Perkin Elmer, model LS 55). Before measurements, the samples were diluted with water and placed in a 10 × 10 mm quartz cuvette. The excitation wavelength was set to 338 nm, with excitation and emission slit widths of 10 nm and a scan speed of 200 nm min^{-1}. The photoluminescence intensity of 7-OHC was recorded at $\lambda = 456$ nm.

The same reactor and experimental conditions were used for the $ABTS^{\bullet+}$ assay. Here, 1 mL of the prepared $ABTS^{\bullet+}$ solution was diluted with ultrapure water in a 50 mL flask. The samples of the aqueous phase were analyzed by UV–Vis spectroscopy (Perkin Elmer, model Lambda 465) using a TrayCell cuvette (Hellma, dilution factor 5, path length 2 mm). The decrease of $ABTS^{\bullet+}$ and the increase of ABTS absorption peaks were observed at 415 nm and 340 nm, respectively.

We used BPA as a model pollutant at a concentration of 10.0 mg/L to investigate the activity of the photocatalysts studied for the degradation of organic pollutants dissolved in water. The concentration of the added catalyst was 125 mg/L. The oxidation of the pollutant was carried out in a 250 mL batch reactor (Lenz laborglas, model LF60) at a temperature of 25 °C and atmospheric pressure. The temperature was kept constant throughout the course of the reaction using a cooling device (Julabo, model F25/ME), while the reaction suspension was continuously aerated with air at a flow rate of 750 mL/min. After the first 30 min in the dark, the system was irradiated with visible light (Philips, 150 W, $\lambda_{max} = 520$ nm). Sampling was performed similarly to other catalytic reactions by filtering the samples through a 0.2 μm membrane filter. The samples in aqueous phase were then analyzed using an HPLC instrument (Shimadzu, model LC-40) operating in isocratic mode. The column (100 × 4.6 mm BDS Hypersil C18, 2.4 μm) was thermostatted to 30 °C and a mixture of methanol and ultrapure water (70 %:30 %, v/v) was used as the mobile phase at a flow rate of 0.5 mL/min. Detection was performed with a PDA detector in the wavelength range between 190 and 350 nm. The device was calibrated daily in the range of 0–20 mg/L BPA with reference solutions.

3. Results and discussion

3.1. Characterization of materials

The main objective of this study was to investigate the effects of different sizes of Au NPs deposited on TNR on photocatalytic activity. Transmission electron microscopy (TEM) was used to investigate the size and dispersion homogeneity of the Au NPs (Figs. 1 and 2) on the TNR support. Modifications of the synthesis protocol enabled the preparation of Au NPs with a relatively narrow size distribution. The TEM micrographs and the size distributions of the Au NPs of Au1, Au2, Au3, Au4 and Au5 are shown in Figs. 1 and 2. The analysis revealed that the Au NPs maintained their size after deposition on the TNR support, indicating high colloidal stability, homogeneous distribution on the TNR support and a well-controlled synthesis process (Table 1). The size distribution is also uniform for all NPs. The significant size differences between the samples are also reflected in their optical appearance: the sample with 10 nm Au NPs (TNR + Au1) had a deep purple colour, while the sample with 50 nm NPs (TNR + Au5) had a lighter, pink colour (see Fig. S2).

Quantitative analysis by scanning electron microscopy with energy-dispersive X-ray spectroscopy (SEM-EDXS) confirmed that the Au loading in all samples was approximately 1.0 wt% (Table 2). Complementary CHN elemental analysis revealed an elevated carbon content in the Au-containing samples compared to bare TNR, suggesting the presence of Na-citrate residues from the synthesis process, which could potentially affect the catalytic activity of the material (Table 2). Nitrogen adsorption–desorption measurements in Fig. 3 and Table 1 showed that the bare TNR support had a S_{BET} of 106 m^2/g and a total pore volume of 0.48 cm^3/g. After deposition of Au NPs, the S_{BET} decreased slightly to 82–91 m^2/g, and the V_{pore} dropped to 0.38–0.41 cm^3/g, while the average d_{pore} (~18.5 nm) remained essentially unchanged. These findings imply that Au NPs slightly blocked the pores of TNR. Due to the nature of TiO_2, the porosity measured in the samples is most likely attributable to interparticle rather than intraparticle pores [30]. The prepared catalysts exhibit N_2 adsorption–desorption isotherms corresponding to type IV according to the IUPAC classification [31], placing them among mesoporous materials with pore sizes ranging from 2 to 50 nm. The typical curve shape at $p/p_0 = 1$ further indicates the presence of pores larger than 50 nm, i.e., macropores [32].

X-ray diffraction (XRD) analysis provided further structural insights (Fig. 4). The diffraction pattern of pristine TNR matched well with the characteristic peaks of anatase TiO_2 described in the literature [33], confirming its crystalline phase. No shifts in peak positions or significant changes in intensity were observed after the deposition of Au, indicating that the anatase structure remained stable. In Au-decorated samples (TNR + Au1 to TNR + Au5), additional peaks appeared at ~32° and ~ 45°. The peak at ~ 32° is attributed to Na_2O [34], a residual by-product from the Na-citrate used in the synthesis of the Au NP, while the peak at ~ 45° corresponds to metallic Au. The peak associated with Au was more pronounced in samples with larger NPs. Therefore, the crystallite size could only be calculated for two TNR + Au samples. In samples TNR + Au4 and TNR + Au5 the Au crystallite size was 16.8 nm for both materials. The anatase crystallite sizes were calculated using the Scherrer equation for comparative purposes only, as this equation is strictly applicable to spherical particles, which nanorods are not (see Table 1).

In order to improve the photocatalytic activity of TNR in the visible-light range, plasmonic Au NPs were applied to its surface. The bare TNR has a wide band gap of 3.2 eV (Fig. 5), which leads to optical absorption only in the UV range. In contrast, the Au-modified samples show a distinct absorption feature between 500–600 nm in the UV–Vis DR spectra, which is due to the LSPR of the Au NPs. The absorption peaks are symmetric and broad, which is consistent with the spherical morphology of the NPs as confirmed by TEM analysis (Fig. 1). Interestingly, the LSPR peak for TNR + Au1 appears at 555 nm, while it is slightly shifted to the blue at 537 nm for the larger Au-decorated samples. While an increase in NP size typically leads to a red shift of the LSPR maximum due to longer plasmon oscillation wavelengths and stronger dielectric interactions, the opposite trend observed here emphasizes the influence of additional factors. In particular, the higher density of smaller Au NPs on the TNR surface and the presence of residual Na-citrate ligands alter the local dielectric environment and enhance the plasmonic coupling between the particles, leading to a pronounced red shift for TNR + Au1. This observation shows that the optical properties of plasmonic photocatalysts are determined not only by the particle size but also by their spatial distribution, surface chemistry and interactions with the support, highlighting the complex interplay of structural and chemical parameters in tailoring the absorption of visible light.

To further explore charge carrier dynamics, photoluminescence (PL) measurements were performed with excitation at 300 nm to efficiently generate e^--h^+ pairs in TNR. As seen in Fig. 6 the Au-modified samples exhibit significantly quenched PL intensities compared to bare TNR, indicating suppressed charge carrier recombination. This suppression is beneficial for photocatalytic activity, as it extends the lifetime of photogenerated charge carriers. Additionally, a slight blue shift in the PL emission peaks from 3.19 eV (TNR) to 3.25 eV (TNR + Au) was observed. This shift can be attributed to the suppression of indirect phonon-assisted transitions in anatase TiO_2 due to the presence of Au NPs [35]. However, the observed peak is characteristic of anatase TiO_2 [36].

The fluorescence lifetime results from the TCSPC measurements are shown in Fig. 7 and Table 3. The excitation/emission cycles were repeated 10,000 times to generate histograms of photon number over time to allow extraction of decay curves and calculation of lifetimes. The peak at ~ 25 ns corresponds to the arrival time of the photons at the detector. To ensure accuracy, the IRF (Instrument Response Function) was calibrated with a Ludox solution and multi-exponential fits were performed with Felix FL software. The TCSPC measurements were performed at three emission wavelengths, with the excitation set at 495 nm. At 350 nm, the bare TNR exhibited a fluorescence lifetime of ~ 0.2 ns, which is consistent with literature reports for TiO_2 [37]. Similar lifetimes were observed for TNR + Au samples, indicating rapid recombination of the photogenerated e^--h^+ pairs and confirming that hot electrons injected from Au NPs into TiO_2 recombine rapidly, similar to electrons in bare TiO_2. Remarkably, a weak fluorescence response is also observed in bare TiO_2 at all three wavelengths, which can be attributed to the presence of defects and Ti^{3+} centers, as confirmed by EPR analysis (see below). These defect states can absorb visible light, leading to emission even in the absence of Au NPs. At 550 nm, the TNR + Au samples showed broader responses and extended lifetimes from 6.09 to 12.8 ns, depending on the size of the Au NPs. This apparent lifetime extension is attributed to plasmonic cloud oscillations that influence the measured signal. In contrast, the measurements at 600 nm reflect the

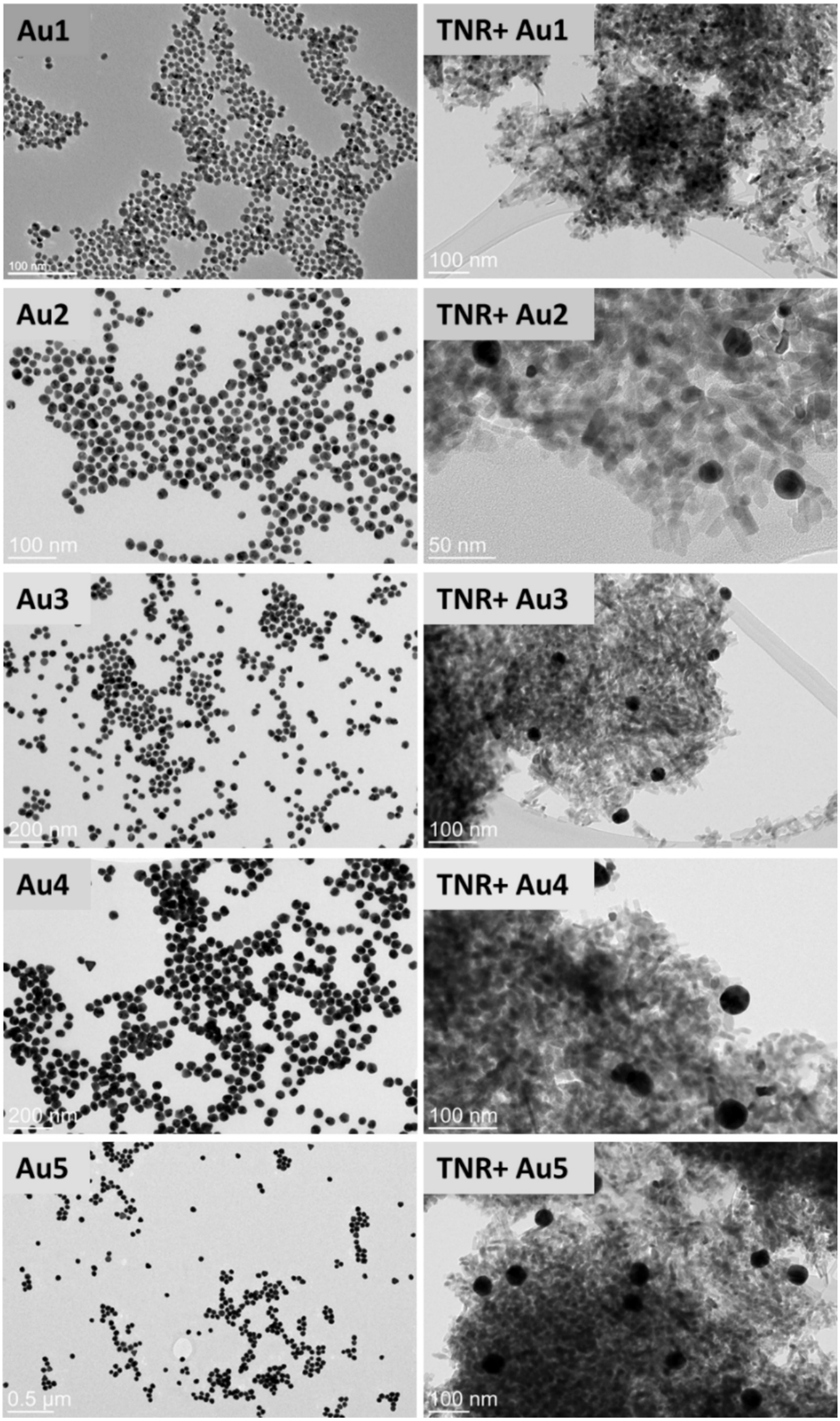

Fig. 1. Overview TEM micrographs of Au NPs and Au/TiO_2 catalysts.

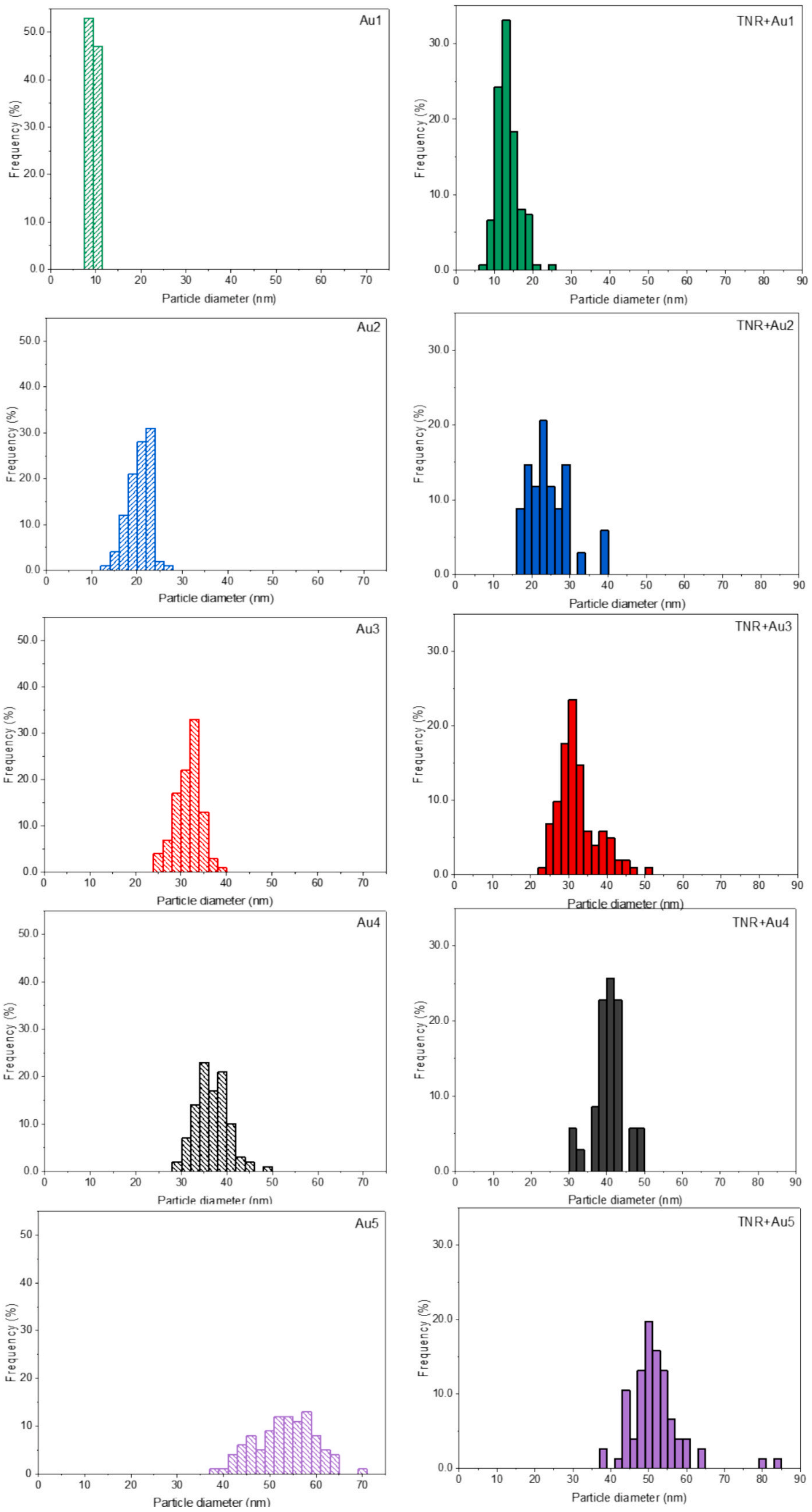

Fig. 2. Particle size distribution of Au NPs and Au ensembles over the TNR support in catalyst samples TNR + Au1, TNR + Au2, TNR + Au3, TNR + Au4 and TNR + Au5. For each sample, the size distribution was obtained from measurements of over 100 independently selected Au NPs.

Table 1

Results of N_2 physisorption (specific surface area (S_{BET}), pore volume (V_{pore}), and pore diameter (d_{pore})), XRD (the apparent crystallite size of anatase and the crystallite size of gold particles were calculated from the diffraction peaks at 25 and 45°, respectively, using the Scherrer equation) and TEM (average size of Au NPs) analyses of the investigated TNR support and TNR + Au catalysts.

Sample	TNR	TNR+ Au1	TNR+ Au2	TNR+ Au3	TNR+ Au4	TNR+ Au5
S_{BET} (m^2/g)	106	82	87	91	86	85
V_{pore} (cm^3/g)	0.48	0.38	0.41	0.41	0.39	0.40
d_{pore} (nm)	18.3	18.7	18.6	18.1	18.4	18.7
[a]Apparent anatase crystallite size (nm)	19.7	19.7	19.7	19.7	21.3	21.3
Au crystallite size (nm)	–	–	–	–	16.8	16.8
[b]Average size of Au NPs (nm)	–	10 ± 1	20 ± 2	31 ± 2	37 ± 4	53 ± 4.5
[c]Average size of Au NPs (nm)	–	13 ± 1	22 ± 2	32 ± 2.5	39 ± 3	52 ± 5

[a] The apparent values were calculated because the TNR support is non-spherical.

[b] The average size of Au NPs before deposition on the TNR support.

[c] The average size of Au NPs after deposition on the TNR support.

Table 2

Results of SEM-EDXS and C-content analysis of the investigated TNR support and Au/TiO_2 catalysts.

Sample		TNR	TNR + Au1	TNR + Au2	TNR + Au3	TNR + Au4	TNR + Au5
Ti	wt. %	67.6 ± 0.3	57.9 ± 0.3	66.1 ± 0.3	61.0 ± 0.3	62.8 ± 0.3	61.4 ± 0.3
O		32.4 ± 0.3	41.0 ± 0.3	32.9 ± 0.3	37.8 ± 0.3	36.0 ± 0.3	37.4 ± 0.3
Au		–	1.1 ± 0.2	1.0 ± 0.2	1.2 ± 0.2	1.2 ± 0.2	1.2 ± 0.2
C		0.2	0.7	0.7	0.5	0.6	0.6

Analysis conditions: voltage 15 keV, ZAF correction method. The instrument was calibrated with an analytical mono-block from MAC.

intrinsic lifetimes of the hot electrons, which are only minimally influenced by the plasmonic cloud. Importantly, the lifetimes of hot electrons in TNR + Au samples remain nearly constant (0.31–0.38 ns, Table 3) over Au NP sizes from 13 to 52 nm (factor 4, Table 1), suggesting that NP size does not significantly affect recombination dynamics in this range. Comparison of TNR + Au samples with different sizes of Au NPs revealed no clear trend in the fluorescence lifetime, suggesting that photocatalytic activity is determined by the number of Au NPs on the TNR surface rather than the lifetime alone. Hot electrons in particular can participate in surface reactions: while still on the Au NPs, they can react with molecular oxygen or organic pollutants such as BPA, and after injection into TiO_2, they can further interact with oxygen and generate reactive oxygen species (ROS).

The ATR-FTIR spectra (Fig. 8) provide insight into surface functional groups and residual species from synthesis. All samples display characteristic bands of TNR, while additional bands at 1585 cm^{-1} and 1389 cm^{-1} correspond to asymmetric and symmetric stretching vibrations of carboxylate groups [38,39], indicating the presence of residual Na-citrate. For the TNR + Au samples the peaks are shifted, which we attribute to interaction of the Au NPs with the carboxyl groups (from adsorbed Na-citrate). Minor peaks at 2902 cm^{-1} and 2982 cm^{-1} [40] are also observed in the TNR + Au samples, further confirming traces of citrate (CH-stretching vibrational modes). Notably, the intensity of these peaks decreases with increasing Au NP size, consistent with the fact that larger Au particles were synthesized with lower amounts of Na-citrate. Furthermore, the ATR-FTIR spectra of the catalysts exhibit a broad band around 3400 cm^{-1}, attributed to O–H stretching vibrations, and a peak at 1640 cm^{-1}, assigned to H-O–H bending. Both features indicate the presence of adsorbed water on the surface of bare TNR and TNR + Au samples.

Thermogravimetric (TG) analysis was performed up to 600 °C to evaluate the thermal stability of the samples and to detect residual organic species from the synthesis (Fig. 9). The bare TNR showed a small weight loss of 2.2 %, which was due to the desorption of physisorbed water and hydroxyl groups. In contrast, the TNR + Au samples showed slightly higher weight losses, ranging from 3.2 % for TNR + Au1 to 2.7 % for TNR + Au5. This trend indicates that the samples containing smaller Au NPs retained more Na-citrate residues (also observed in the CHN analysis, Table 2) from the synthesis process, which were not completely removed during drying and calcination. For TNR + Au1, the TG curve showed a decreasing slope beyond 400 °C, indicating that most of the organic residues had decomposed at this temperature, although mass loss continued slowly up to 600 °C. The lowest overall mass loss was observed for sample TNR + Au5, indicating that fewer organic stabilizers were present in the catalyst. These results are consistent with the ATR-FTIR spectra (Fig. 8), where citrate-related peaks were more pronounced in samples with smaller Au NPs. To conclude, the TG results confirm the presence of residual synthesis by-products on the catalyst surface.

Overall, the above results consistently show the influence of residual Na-citrate introduced during the synthesis of Au NPs. Smaller Au NPs required higher amounts of citrate as a stabilizing agent, which explains the higher carbon content in the CHN analysis, the more intense carboxylate bands in the ATR-FTIR spectra and the larger weight losses in TG measurements. The dielectric effect of the adsorbed citrate species also contributes to the unusual red shift of the LSPR band in samples with smaller Au NPs, indicating that not only the particle size but also the chemical environment determines the optical response. These results highlight that while citrate residues are essential for stabilizing the NPs, they can alter the structural, optical and potentially catalytic properties of the TNR + Au materials. Although the total citrate content in the samples is only about 1 wt%, its influence is considerable, because catalysis and plasmonic absorption are very surface-sensitive phenomena.

Electron paramagnetic resonance (EPR) spectroscopy was employed to investigate the paramagnetic centers in hydrothermally prepared TNR and in Au-decorated TNR catalysts. To monitor the light-induced formation of paramagnetic species, the EPR spectra were recorded in the dark and under irradiation with visible light (Fig. 10) for TNR and TNR + Au samples at room temperature (RT). In the case of TNR, the P1 signal is assigned to Ti^{3+} ions and may also reflect the presence of oxygen vacancies (P2) [41–43], as already shown by PL analysis (Fig. 6). The broad P1 + P2 features indicate that most Ti^{3+} centers are located at the TNR surface [41,44]. In addition, the P4 signal confirms the presence of bulk Ti^{3+}, originating from hydrothermal synthesis that generates oxygen vacancies at the surface; charge balancing then requires the formation of additional Ti^{3+} species. The P3 signal can be attributed either to the rhombic component of the O_2^- species [41,45]. The same spectral response was observed when a yellow optical filter was used (Figs. S1 and S3a). The emission spectrum of the LED illumination source (Fig. S1) shows maxima at ~ 450 and ~ 520 nm, corresponding to photon energies below the TiO_2 band gap (3.2 eV). This confirms that TiO_2 cannot be directly excited across its band gap under the experimental conditions. Instead, illumination only addresses the Au NPs via LSPR. The sharp instrumental feature at $g \approx 2.00$ was also present in cavity baseline measurements and therefore does not originate from the samples. The EPR intensity increases in Au-decorated samples, although it varies between different samples depending on the presence of Na-citrate and the size of the Au NPs. Solid-state EPR measurements performed for Na-citrate alone (Fig. S3b) showed that it was unexpectedly EPR-silent. However, the reaction between Na-citrate and TNR may result in surface contamination that suppresses the ability of the Ti^{3+} centers on the surface to participate in visible-light processes. In addition, Na-citrate may be present at the Au/TNR interface, which

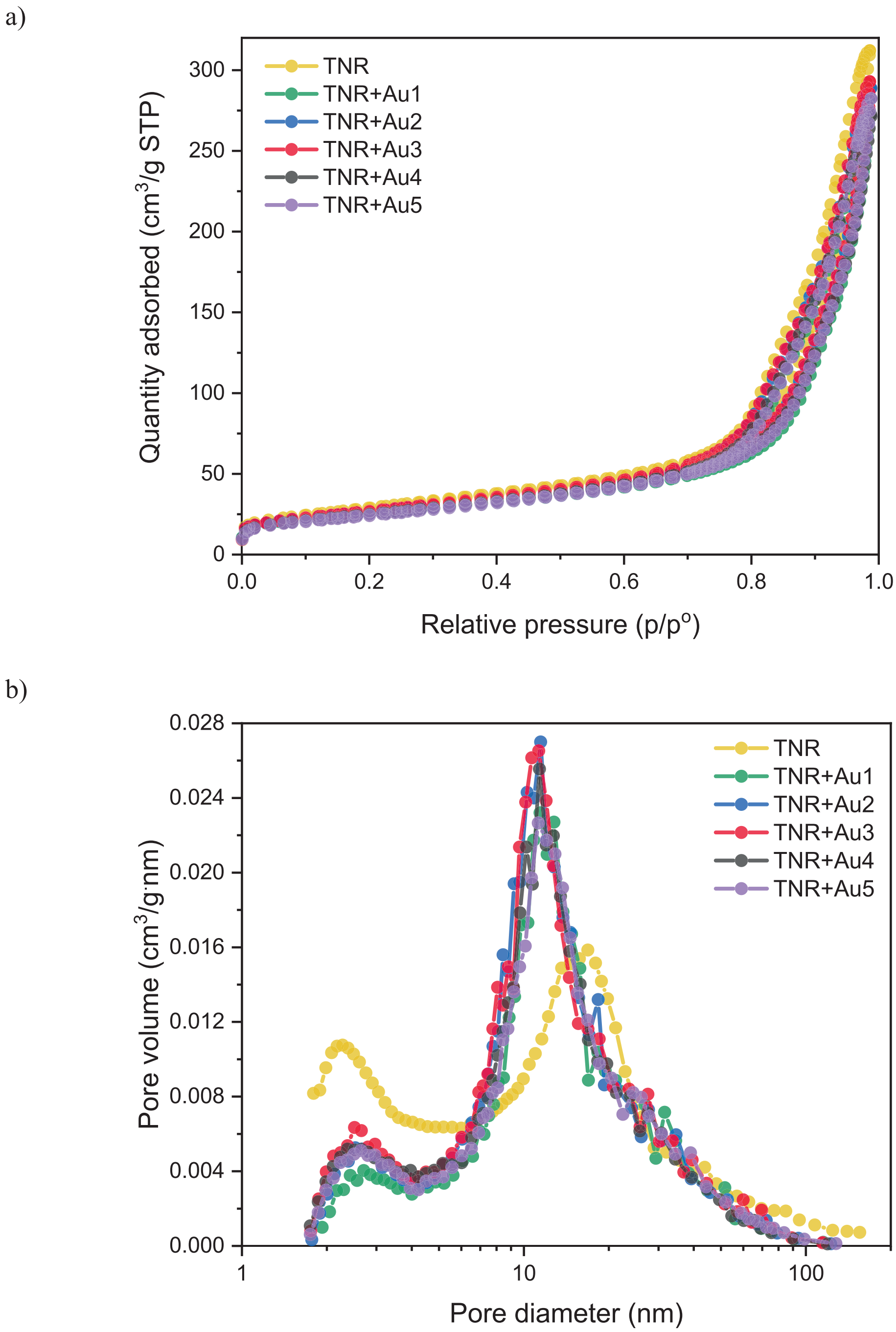

Fig. 3. a) Nitrogen adsorption/desorption isotherms and b) corresponding BJH pore size distribution for catalysts, with and without gold NPs.

negatively affects the carrier mechanism. Importantly, a comparison of the EPR spectra of the TNR + Au series shows that the spectral features are essentially the same, but their relative intensities are slightly different. In the Au-decorated samples, the P1/P2 resonances appear enhanced compared to bare TNR. These variations correlate with differences in the size of the Au NPs and the amount of residual Na-citrate, both of which may influence the stabilization or suppression of the Ti^{3+} centers at the surface. Taken together, these observations show that Au decoration alters the steady-state EPR response, but illumination with the full LED spectrum or with yellow-filtered light does not significantly increase the concentration of long-lived Ti^{3+} or vacancy-related centers compared to the dark state. The presence of Au affects the baseline intensity of Ti^{3+}-related signals, but not their sensitivity to light. This suggests that plasmonic excitation of Au NPs generates hot carriers, but that these carriers either recombine on ultrafast timescales or follow pathways that do not terminate in long-lived EPR-detectable Ti^{3+} or oxygen-vacancy species. The residual Na-citrate, detected by FTIR and TG analyses, likely further modulates this behaviour by blocking or passivating TiO_2 surface sites. Thus, the EPR results highlight two important points: (i) Au decoration and surface chemistry affect the initial concentration of stabilized Ti^{3+} centers, leading to small differences in intensity within the TNR + Au series, and (ii) visible-light illumination, whether filtered or unfiltered, does not lead to additional enrichment of long-lived paramagnetic species at room temperature.

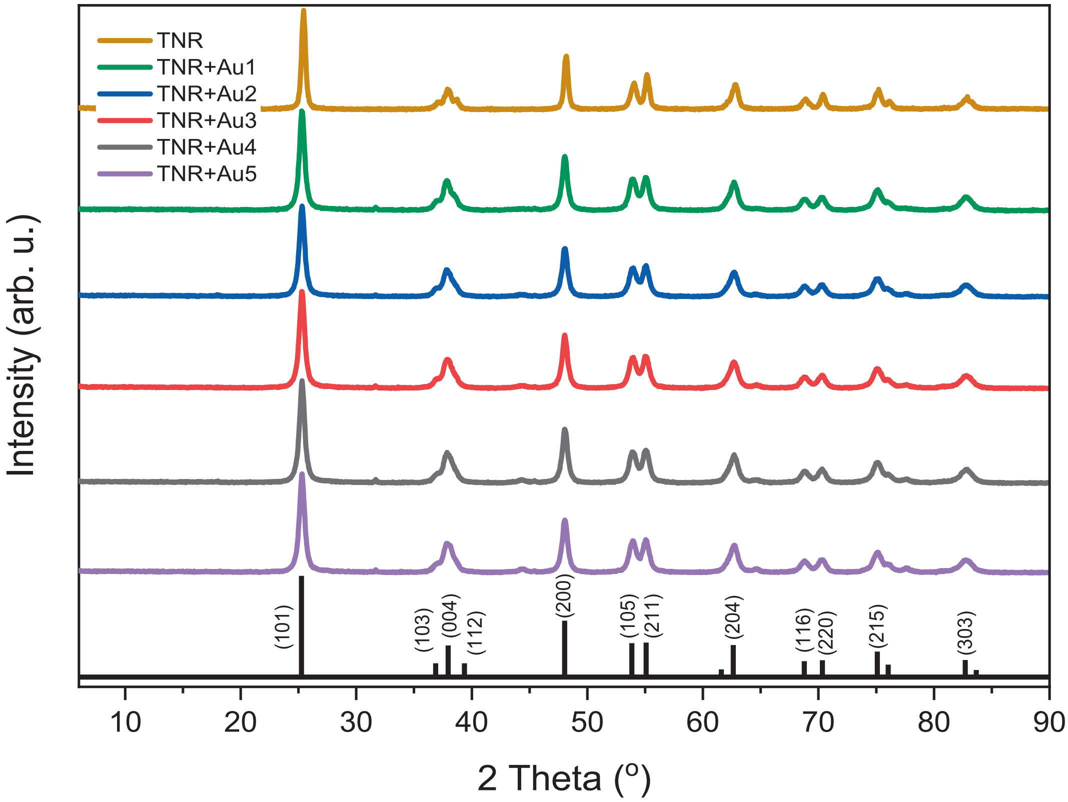

Fig. 4. XRD diffractograms of the TNR support and catalysts containing 1.0 wt% of Au loading. Anatase and gold crystallite sizes are listed in Table 1.

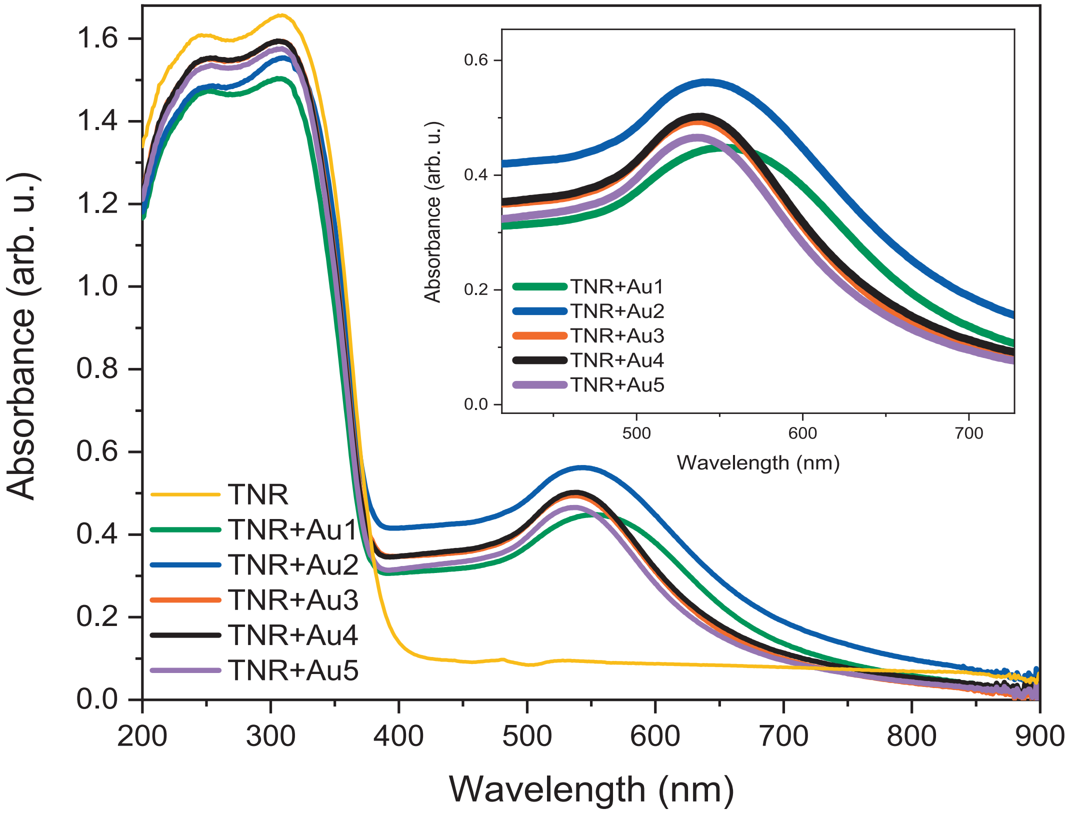

Fig. 5. UV–Vis DR spectra of the TNR support and catalysts containing 1.0 wt% of Au.

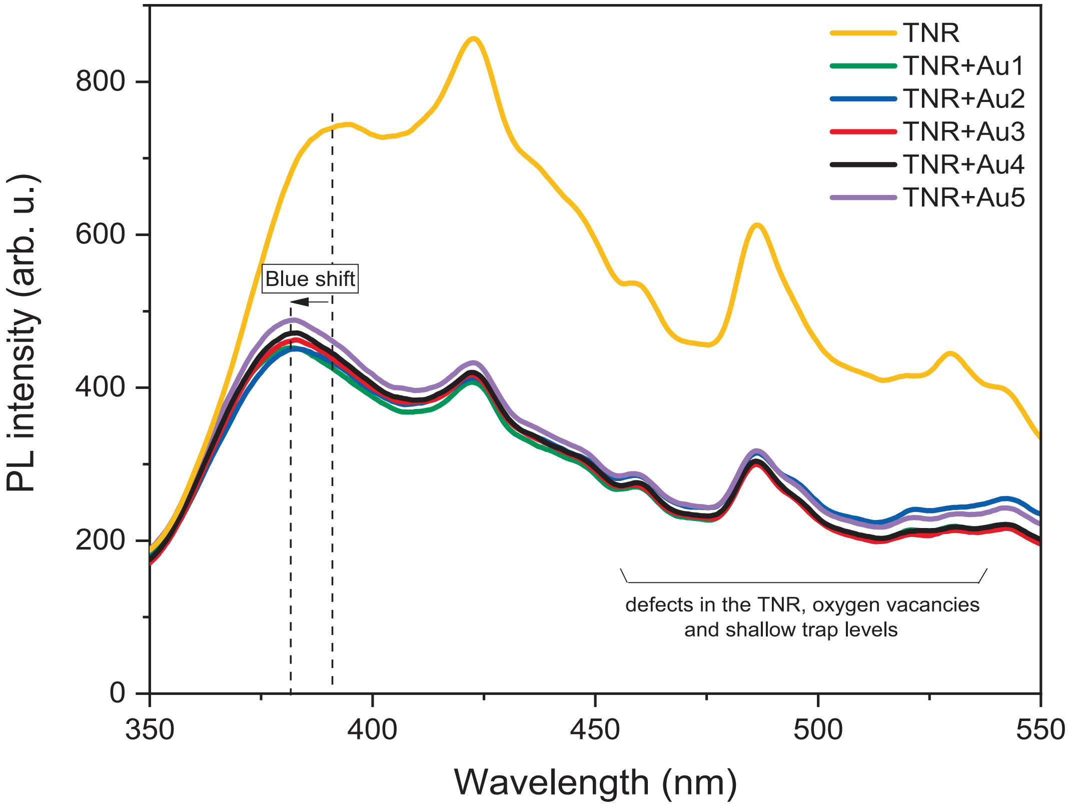

Fig. 6. Solid-state photoluminescence (PL) emission spectra of the investigated materials.

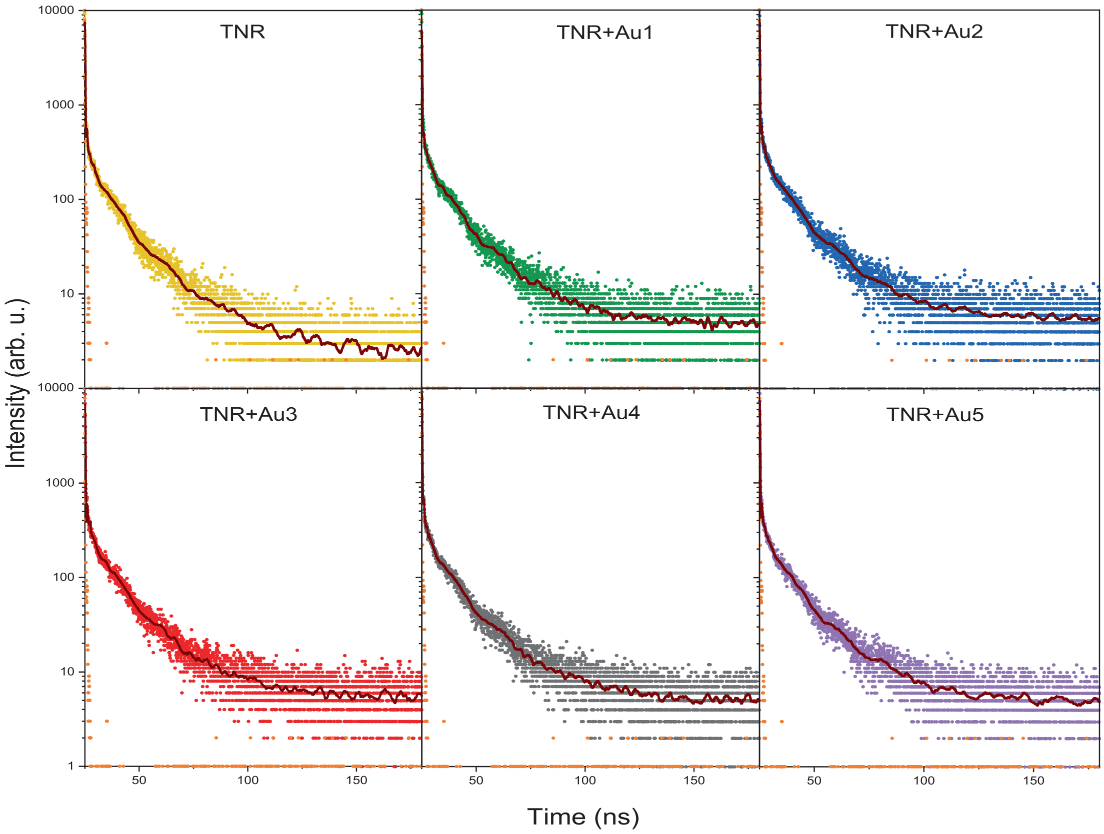

Fig. 7. Time-correlated single photon counting (TCSPC) measurements of the TNR support and TNR + Au catalysts. The orange signal is an IRF response and the dark red curve represents the exponential fit of the measured signals of the samples.

Table 3
Results of fluorescence lifetime and χ^2 value for catalysts obtained by TCSPC analysis.

Sample		TNR	TNR + Au1	TNR + Au2	TNR + Au3	TNR + Au4	TNR + Au5
Fluorescence lifetime (ns)	$\lambda_{em.}$ = 350 nm	0.26	0.14	0.14	0.13	0.11	0.16
χ^2 (/)		1.35	1.09	1.22	1.17	1.15	1.25
Fluorescence lifetime (ns)	$\lambda_{em.}$ = 550 nm	2.81	7.2	10.6	12.8	9.75	6.09
χ^2 (/)		1.89	1.25	2.04	1.24	2.11	1.97
Fluorescence lifetime (ns)	$\lambda_{em.}$ = 600 nm	0.20	0.37	0.33	0.38	0.31	0.38
χ^2 (/)		1.19	1.22	1.19	1.15	1.3	1.2

3.2. *Catalytic activity*

Photocatalytic tests were performed to evaluate the activity of the materials against model pollutants. Initially, ABTS$^{\bullet+}$ and coumarin (COUM) reactions were carried out to identify the types of reactive oxygen species (ROS) generated by the photocatalysts containing Au NPs of varying sizes. In the ABTS$^{\bullet+}$ assay (Fig. 11), the formation of $O_2^{\bullet-}$ and e^- was monitored by measuring the temporal concentration of ABTS$^{\bullet+}$ at 415 nm [46]. The lowest relative concentration of ABTS$^{\bullet+}$ was observed for the TNR + Au1 sample, which contains the smallest Au NPs. This indicates the highest generation of e^- and $O_2^{\bullet-}$ radicals by this catalyst. Conversely, the sample with the largest Au NPs exhibited the lowest ROS formation.

The COUM reaction, also conducted under visible-light illumination, enabled detection of OH$^\bullet$ radicals through the fluorescent product 7-hydroxycoumarin (7-OHC), measured at 452 nm [47]. Although this only accounts for part of the total OH$^\bullet$ generated (since other products cannot be directly measured via fluorescence), the results (Fig. 12) revealed a similar trend: TNR + Au1 exhibited the highest formation of OH$^\bullet$ radicals, while the other samples showed a significantly lower, but comparable and size-independent behavior.

For the photocatalytic degradation of a model pollutant, BPA at a concentration of 10.0 mg L^{-1} (similar to levels found in landfill leachates), experiments were conducted over 4 h (Fig. 13). An initial 30-minute dark phase confirmed negligible adsorption of BPA on the catalyst surface. A control test without catalyst also showed no BPA photolysis under visible light. After illumination, the bare TNR showed minimal photocatalytic response, as expected given the large band gap of TiO_2 and its inactivity under visible light. However, the low activity of TNR is attributed to surface defects and Ti^{3+} species, which can easily extend the light absorption into the visible region. The TNR + Au1 catalyst achieved ~ 40 % BPA degradation, clearly outperforming the other TNR + Au samples, which showed similar but significantly lower activity. Although TNR + Au1 achieved ~ 40 % degradation in 4 h, this performance can be considered satisfactory compared to other studies with the same Au size [21], considering the much lower catalyst loading and shorter irradiation time in our experiments.

It is important to note that even TNR + Au samples did not display high photocatalytic efficiency overall. This limitation is most likely caused by residual Na-citrate used during synthesis, which remains adsorbed on the catalyst surface. The presence of citrate residues inhibits access of pollutant molecules to active sites, thereby constraining

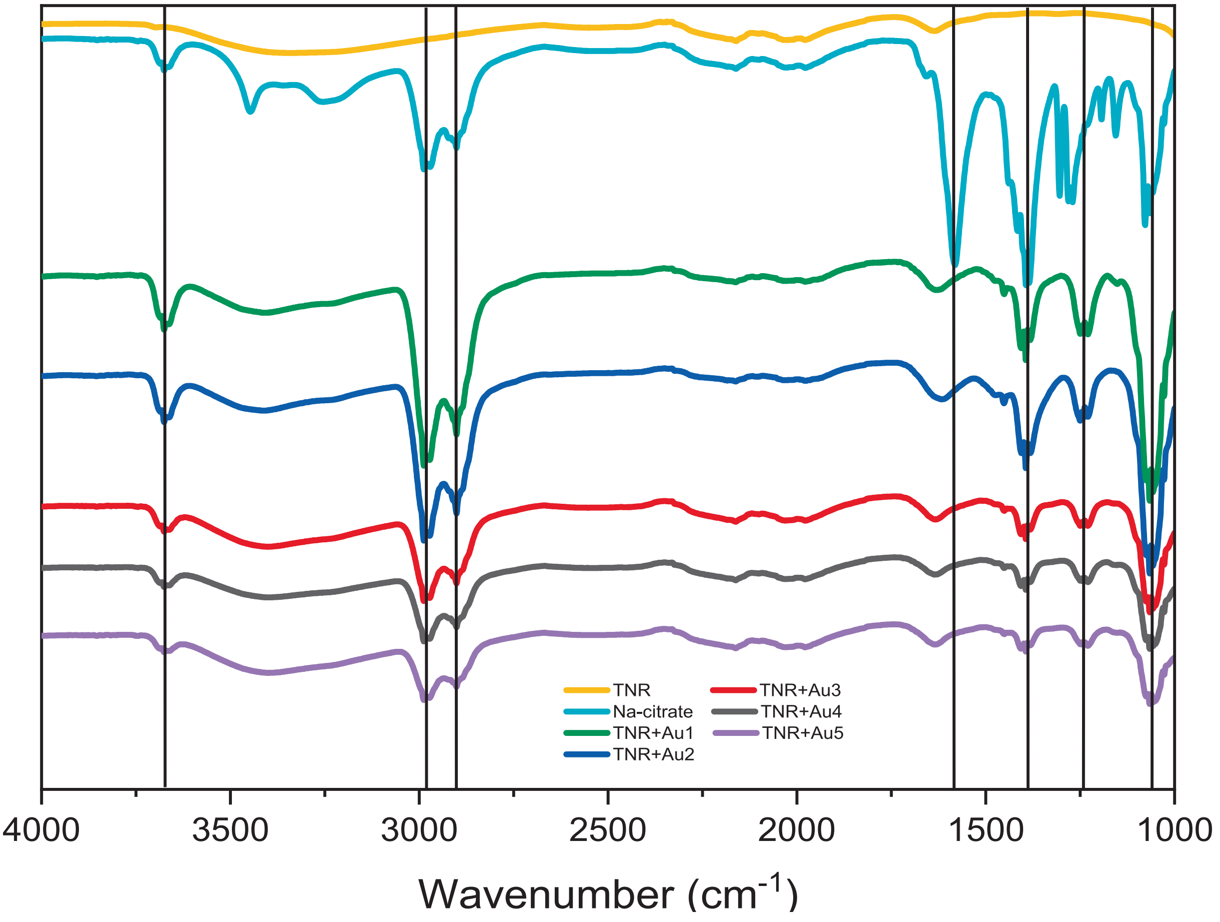

Fig. 8. ATR-FTIR spectra of Na-citrate, TNR support and TNR + Au catalysts containing 1.0 wt% of Au loading.

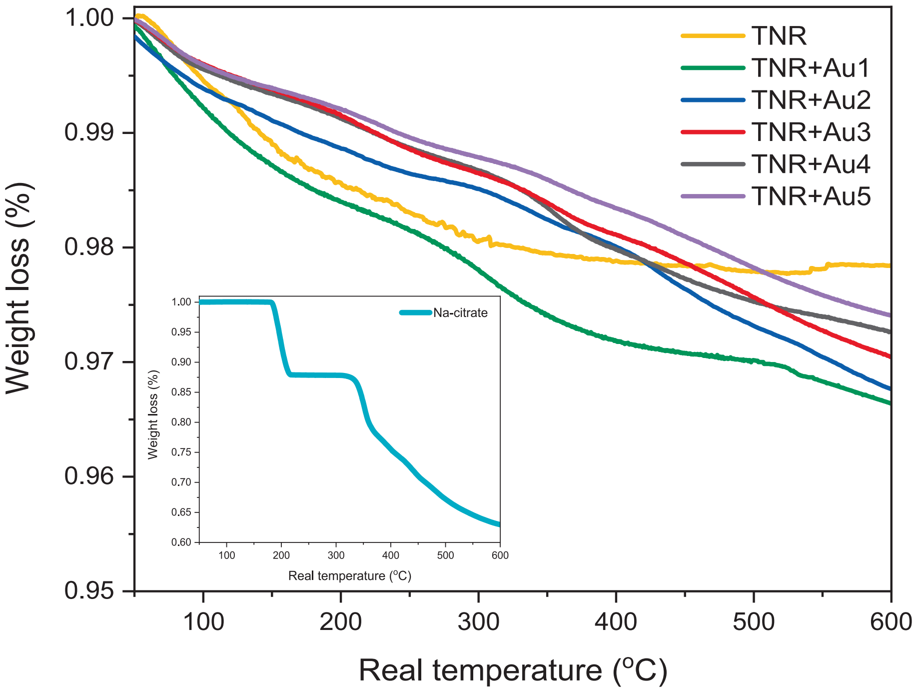

Fig. 9. The TGA thermographs of pure TNR and TNR + Au catalysts.

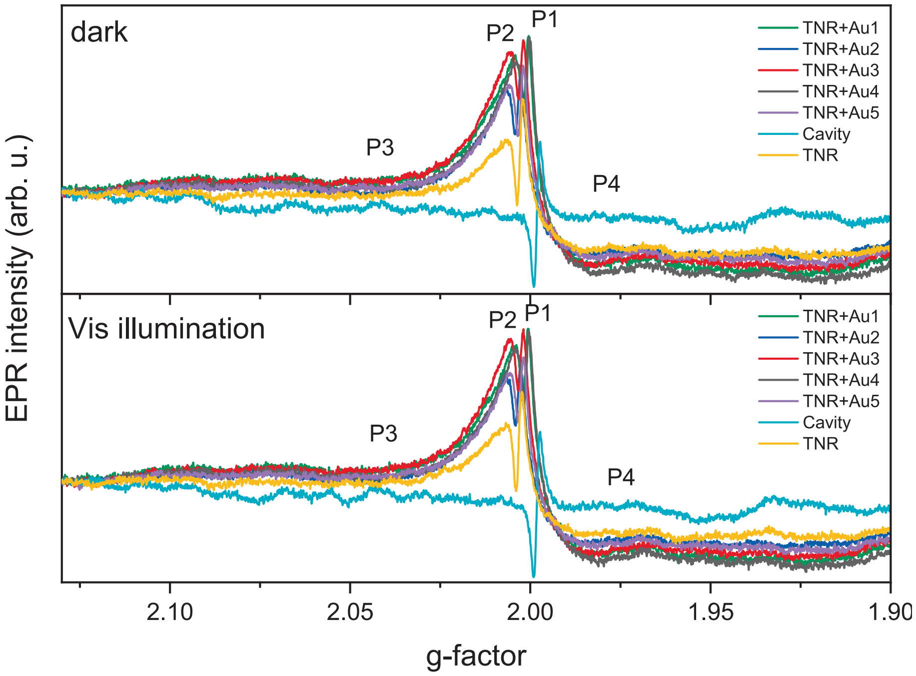

Fig. 10. Solid-state EPR spectra of the analyzed samples recorded in the dark and under illumination with visible light at room temperature (RT).

the catalytic response. Despite this, a clear trend was observed where photocatalytic activity increased as Au NP size decreased, likely due to the higher number of smaller NPs (as confirmed by TEM analysis, Figs. 1 and 2).

4. Conclusions

Using our synthesis and decoration methods, Au NPs of different sizes were successfully deposited on TNR. The smallest Au NPs were obtained in the TNR + Au1 sample, while TNR + Au5 contained the largest ones. The Au NPs exhibited a narrow size distribution and maintained their dimensions after deposition, ensuring high colloidal stability. This colloidal stabilization was made possible by the presence of Na-citrate. However, the residual citrate proved to be a critical factor affecting both surface chemistry and catalytic performance.

Optical characterization confirmed the introduction of plasmonic properties, with the Au-modified samples exhibiting LSPR in the visible region. Unexpected spectral shifts were observed, especially in TNR + Au1, where the red shift of the LSPR band was related to the higher number of Au NPs and the presence of residual citrate. PL and TCSPC

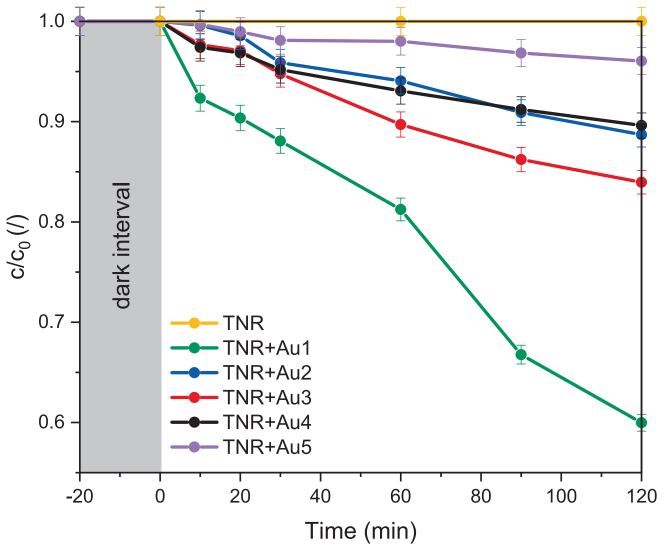

Fig. 11. Relative concentration of ABTS$^{\bullet+}$ as a function of time obtained in the presence of investigated photocatalysts under visible-light illumination.

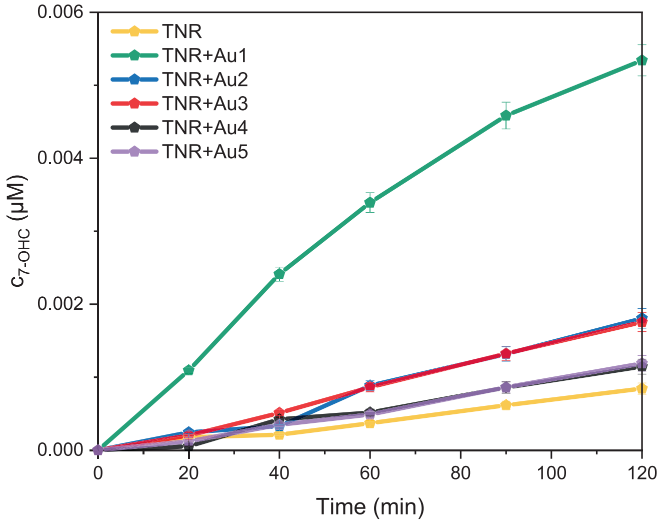

Fig. 12. Dependence of 7-hydroxycoumarin (7-OHC) concentration on irradiation time, measured upon visible-light illumination of aqueous suspensions containing investigated catalysts and coumarin (COUM).

measurements showed that Au decoration suppressed e^--h^+ recombination and prolonged carrier lifetime. Nevertheless, this effect was not the primary determinant of photocatalytic activity. EPR spectroscopy provided further insight into defect-related processes and confirmed the stabilization of Ti^{3+} centers and oxygen vacancies, both of which contribute significantly to visible-light activity.

Photocatalytic tests showed a clear size-dependent trend: catalysts decorated with smaller Au NPs (TNR + Au1) exhibited the highest ROS formation and the best BPA degradation when irradiated with visible light. This improvement was attributed to the higher number of small Au NPs, which act as efficient charge separation and transfer sites. In contrast, the samples with larger Au NPs showed lower activity, although they had similar structural and optical properties. These results strongly suggest that the photocatalytic performance of Au/TNR systems is primarily determined by the number of Au NPs and not only by the lifetime.

Despite these promising observations, the overall photocatalytic activity of the Au/TiO_2 catalysts remained modest. Residual Na-citrate was identified as a limiting factor, adsorbing on the catalyst surface, hindering charge transfer and blocking access of the pollutant molecules to the active sites. This underlines the need to optimize post-synthesis purification (e.g., calcination, washing protocols) or to develop alternative capping agents that can be removed more easily without compromising the stability of the NPs.

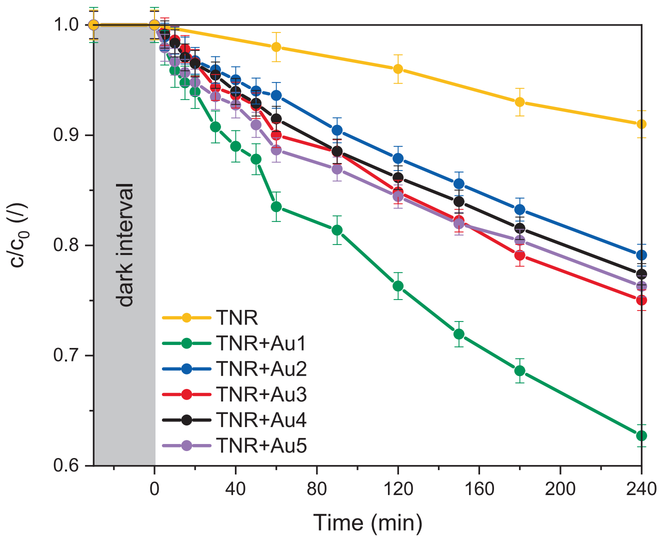

Fig. 13. Photocatalytic degradation of BPA dissolved in water ($V = 250$ mL, $c_0 = 10.0$ mg/L) under visible-light illumination at $T = 25$ °C in the presence of pure TNR support and Au/TiO_2 catalysts (125 mg/L). The first 30 min of the reaction were dark to eliminate adsorption.

CRediT authorship contribution statement

Špela Slapničar: Writing – original draft, Visualization, Methodology, Investigation. **Maja Caf:** Writing – original draft, Methodology, Investigation. **Slavko Kralj:** Supervision, Resources, Investigation, Funding acquisition. **Gregor Žerjav:** Writing – review & editing, Visualization, Investigation. **Albin Pintar:** Writing – review & editing, Supervision, Resources, Project administration, Methodology, Investigation, Funding acquisition, Conceptualization.

Declaration of competing interest

The authors declare that they have no known competing financial interests or personal relationships that could have appeared to influence the work reported in this paper.

Acknowledgments

The authors acknowledge the financial support from the Slovenian Research and Innovation Agency (ARIS) through the core funding No. P2-0150, P2-0089, ARIS projects: No. J2-60047, J2-3043, J3-3079, J7-4420, L2-60141 and bilateral ARIS projects: BI-FR/23-24-PROTEUS-005 (PR-12039) and BI-RS/23-25-030 (PR-12782). The authors acknowledge the CEMM Nanocenter (JSI, Slovenia) for the access to electron microscopy.

Appendix A. Supplementary data

Supplementary data to this article can be found online at https://doi.org/10.1016/j.apsusc.2025.165300.

Data availability

Data will be made available on request.

References

[1] X.M. Cui, Supply and demand status of bisphenol at home and abroad and its development prospect, Technol. Econ. Petrochem 33 (2017) 17–22.

[2] I. Lee, K.T. Kim, S. Kim, S. Park, H. Lee, Y. Jeong, Bisphenol a exposure through receipt handling and its association with insulin resistance among female cashiers, Environ. Inter. 117 (2018) 268–275.

[3] C.Y. Kuo, C.H. Wu, H.Y. Lin, Photocatalytic degradation of bisphenol a in a visible light/TiO_2 system, Desalination 256 (2010) 37–42.

[4] J.R. Masoner, D.W. Kolpin, E.T. Furlong, I.M. Cozzarelli, J.L. Gray, Landfill leachate as a mirror of today's disposable society: pharmaceuticals and other contaminants of emerging concern in final leachate from landfills in the conterminous United States, Environ. Toxicol. Chem. 35 (2016) 906–918.

[5] T. Yamamoto, A. Yasuhara, Quantities of bisphenol a leached from plastic waste samples, Chemosphere 38 (1999) 2569–2576.

[6] U. Hübner, S. Spahr, H. Lutze, A. Wieland, S. Rüting, W. Gernjak, J. Wenk, Advanced oxidation processes for water and wastewater treatment – guidance for systematic future research, Heliyon 10 (2024) e30402.

[7] A. Chakravorty, S. Roy, A review of photocatalysis, basic principles, processes, and materials, Sustain. Chem. Environ. 8 (2024) 100155.

[8] A. Fujishima, T.N. Rao, D.A. Tryk, Titanium dioxide photocatalysis, J. Photochem, Photobiol. C. 1 (2000) 1-21.

[9] M. Pelaez, N.T. Nolan, S.C. Pillai, M.K. Seery, P. Falaras, A.G. Kontos, P.S. M. Dunlop, J.W.J. Hamilton, J.A. Byrn, K. ÓShea, M.H. Entezari, D.D. Dionysiou, A review on the visible light active titanium dioxide photocatalysts for environmental applications, Appl. Catal. B 125 (2012) 331–349.

[10] C. Dette, M.A. Pérez-Osorio, C.S. Kley, P. Punke, C.E. Patrick, P. Jacobson, F. Giustino, S. Jung, K. Kern, TiO_2 anatase with a bandgap in the visible region, Nano Lett. 14 (2014) 6533–6538.

[11] J. Zhang, X. Suo, J. Zhang, B. Han, P. Li, Y. Xue, H. Shi, One-pot synthesis of Au/TiO_2 heteronanostructure composites with SPR effect and its antibacterial activity, Mat. Lett. 162 (2016) 235–237.

[12] D. Bahnemann, D. Bochelmann, R. Goslich, Mechanistic studies of water detoxification in illuminated TiO_2 suspensions, Sol. Energy Mater. 24 (1991) 564–583.

[13] Y. Huang, X. Xu, G. Fan, X. Zhu, L. Zhu, X. Chen, Effect of TiO_2 crystal phase on the construction of TiO_2/g-C_3N_4 heterojunction photocatalyst for efficient sunlight photodegradation of naphthalene, Colloids Surf A Physicochem Eng Asp 694 (2024) 134170.

[14] I. Hammami, N.M. Alabdallah, A. Al Jomaa, Gold nanoparticles: synthesis properties and applications, J. King Saud Univ. Sci. 33 (2021) 101560.

[15] D.T. Thompson, Using gold nanoparticles for catalysis, Nano Today 2 (2007) 40–43.

[16] L. Lin, Q. Zhong, Y. Zheng, Y. Cheng, R. Qi, R. Huang, Size effect of Au nanoparticles in Au-$TiO_{2\text{-}x}$ photocatalyst, Chem. Phys. Lett. 770 (2021) 138457.

[17] M. Luna, J.M. Gatica, H. Vidal, M.J. Mosquera, Au-TiO_2/SiO_2 photocatalysts with NO_X depolluting activity: influence of gold particle size and loading, Chem. Eng. J. 368 (2019) 417–427.

[18] D. Tsukamoto, Y. Shiraishi, Y. Sugano, S. Ichikawa, S. Tanaka, T. Hirai, Gold nanoparticles located at the interface of anatase/rutile TiO_2 particles as active plasmonic photocatalysts for aerobic oxidation, J. Am. Chem. Soc. 134 (2012) 6309–6315.

[19] S.M. Yoo, S.B. Rawal, J.E. Lee, J. Kim, H.-Y. Ryu, D.-W. Park, W.I. Lee, Size-dependence of plasmonic Au nanoparticles in photocatalytic behavior of Au/TiO_2 and Au@SiO_2/TiO_2, Appl. Catal. A 499 (2015) 47–54.

[20] P. Fu, P. Zhang, Uniform dispersion of Au nanoparticles on TiO_2 film via electrostatic self-assembly for photodegradation of bisphenol a, Appl. Catal. B: Environ. 96 (2010) 176–184.

[21] B. Cojocaru, V. Andrei, M. Tudorache, F. Lin, C. Cadigan, R. Richards, V. I. Parvalescu, Enhanced photo-degradation of bisphenol pollutants onto gold-modified photocatalysts, Catal. Today 284 (2017) 153–159.

[22] G. Žerjav, J. Zavašnik, J. Kovač, A. Pintar, The influence of Schottky barrier height onto visible-light triggered photocatalytic activity of TiO_2+Au composites, Appl. Surf. Sci. 543 (2021) 148799.

[23] G. Žerjav, M.S. Arshad, P. Djinović, J. Zavašnik, A. Pintar, Electron trapping energy states of TiO_2-WO_3 composites and their influence on phoocatalytic degradation of bisphenol a, Appl Catal B 209 (2017) 273–284.

[24] I. Ojea-Jiménez, N.G. Bastús, V. Puntes, Influence of the sequence of the reagents addition in the citrate-mediated synthesis of gold nanoparticles, J. Phys. Chem. C. Nanomater. Interfaces 115 (2011) 15752–15757.

[25] N.G. Bastús, J. Comenge, V. Puntes, Kinetically controlled seeded growth synthesis of citrate-stabilized gold nanoparticles of up to 200 nm: size focusing versus Ostwald ripening, Langmuir 27 (2011) 11098–11105.

[26] T. Polajžer, M. Kranjc, S. Kralj, M. Caf, R. Romih, S. Hudoklin, F. Rocca, D. Miklavčič, Limited efficacy of nanoparticle-assisted electroporation for membrane permeabilization and gene electrotransfer, Pharmaceutics 17 (2025) 964.

[27] Š. Slapničar, G. Žerjav, M. Roškarič, J. Zavašnik, A. Pintar, Variations of electronic properties on the behaviour of visible light-triggered TiO_2+Au photocatalysts, Appl. Surf. Sci. 695 (2025) 162923.

[28] Š. Slapničar, G. Žerjav, M. Németh, J. Zavašnik, A. Pintar, Design and evaluation of plasmonic metal-TiO_2 nanostructure for photocatalytic degradation of BPA as a model pollutant, J. Colloid Interface Sci. 700 (2025) 138361.

[29] P. Verma, K. Mori, Y. Kuwahara, S. June Cho, H. Yamashita, Synthesis of plasmonic gold nanoparticles supported on morphology-controlled TiO_2 for aerobic alcohol oxidation, Catal. Today 352 (2020) 255–261.

[30] M.I. Zaki, N.E. Fouad, G.A.H. Mekhemer, T.C. Jagadale, S.B. Ogale, TiO_2 nanoparticle size dependence of porosity, adsorption and catalytic activity, Colloids Surf. A: Physicochem. Eng. Aspects 385 (2011) 195–200.

[31] F.J. Sotomayor, K.A. Cychosz, M. Thommes, Characterization of micro/mesoporous materials by physisorption: concepts and case studies, Acc. Mater. Surf. Res. 3 (2018) 34–50.

[32] P. Bertier, K. Schweinar, H. Stanjek, A. Ghanizadeh, C.R. Clarkson, A. Busch, N. Kampman, D. Prinz, A. Amann-Hildenbrand, B.M. Krooss, V. Pipich, On the use and abuse of N_2 physisorption for the characterization of the pore structure of shales, CMS Workshop Lect 21 (2016) 151–161.

[33] W. Li, R. Liang, A. Hu, Z.-H. Huang, Generation of oxygen vacancies in visible light activated one-dimensional iodine TiO_2 photocatalysts, RCS Adv. 4 (2014) 36959.

[34] E. García-Bordejé, A.B. Dongil, J. Moral, J.M. Conesa, A. Guerrero-Ruiz, I. Rodríguez-Ramos, Cyclic performance in CO_2 capture-methanation of bifunctional Ru with different base metals: effect of the reactivity of CO_X ad-species, J. CO2 Util. 68 (2023) 102370.

[35] H. Nakajima, T. Mori, M. Watanabe, Influence of platinum loading on photoluminiscence of TiO_2 powder, J. Appl. Phys. 96 (2004) 925–927.

[36] V. Jovic, Z.H.N. Al-Azri, W.T. Chen, D. Sun-Waterhouse, H. Idriss, G.I. N. Waterhouse, Photocatalytic H_2 production from ethanol-water mixtures over Pt/TiO_2 and Au/TiO_2 photocatalysts: a comparative study, Top. Catal. 56 (2013) 1139–1151.

[37] K. Santhosh, S. Sk, S. Chouti, S. Gonuguntla, S.P. Ega, A. Tiwari, U. Pal, Tailoring hierarchical porous TiO_2 based ternary rGO/NiO/TiO_2 photocatalyst for efficient hydrogen production and degradation of Rhodamine B, J. Mol. Struct. 1235 (2021) 130222.

[38] J.J. Max, C. Chapados, Infrared spectroscopy of aqueous carboxylic acids: Comparison between different acids and their salts, J. Phys. Chem. A 108 (2004) 3324–3337.

[39] J.W. Park, J.S. Shumaker-Parry, Structural study of citrate layers on gold nanoparticles: Role of intermolecular interactions in stabilizing nanoparticles, J. Am. Chem. Soc. 136 (2014) 1907–1921.

[40] E. Sritham, S. Gunasekaran, FTIR spectroscopic evaluation of sucrose-maltodextrin-sodium citrate bioglass, Food Hydrocoll. 70 (2017) 371–382.

[41] A.M. Abdel-Mageed, K. Wiese, A. Hauble, J. Bansmann, J. Rabeah, M. Parlinska-Wojtan, A. Brückner, R.J. Behm, Steering the selectivity in CO_2 reduction on highly active Ru/TiO_2 catalysts: support particle size effects, J. Catal. 401 (2021) 160–173.

[42] I. Caretti, M. Keulemans, S.W. Verbruggen, S. Lenaerts, S. Van Doorslaer, Light-Induced Processes in Plasmonic Gold/TiO_2 Photocatalysts Studied by Electon Paramagnetic Resonance, Top. Catal. 58 (2015) 776–782.

[43] J.B. Priebe, M. Karnahl, H. Junge, M. Beller, D. Hollmann, A. Brückner, Water reduction with visible light: synergy between optical transitions and electron transfer in Au-TiO_2 catalysts visualized by in situ EPR spectrocopy, Angew. Chem. Int. Ed. 52 (2013) 11420–11424.

[44] L.-B. Xiong, J.-L. Li, B. Yang, Y. Yu, Ti^{3+} in the surface of titanium dioxide: generation, properties and photocatalytic application, J. Nanomater. 2012 (2011) 831524.

[45] D.C. Hurum, A.G. Agrios, K.A. Gray, T. Rajh, M.C. Thurnauer, Explaining the enhanced photocatalytic activity of degussa P25 mixed-phase TiO_2 using EPR, J. Phys. Chem. B 107 (2003) 4545–4549.

[46] V. Brezová, D. Dvoranová, A. Staško, Characterization of titanium dioxide photoactivity following the formation of radicals by EPR spectroscopy, Res. Chem. Intermed. 33 (2007) 251–268.

[47] G. Louit, S. Foley, J. Cabillic, H. Coffigny, F. Taran, A. Valleix, J.P. Renault, S. Pin, The reaction of coumarin with the OH radical revisted: hydroxylation product analysis determined by flourescence and chromatography, Radiat. Phys. Chem. 72 (2005) 119–124.